Available online at www.sciencedirect.com

ScienceDirect

Acta Materialia 75 (2014) 337–347

Acta MATERIALIA

www.elsevier.com/locate/actamat

Phase-field modeling of martensitic microstructure in NiTi shape memory alloys

Yuan Zhong [a], Ting Zhu [a,b,*]

[a] Woodruff School of Mechanical Engineering, Georgia Institute of Technology, Atlanta, GA 30332, USA
[b] School of Materials Science and Engineering, Georgia Institute of Technology, Atlanta, GA 30332, USA

Received 26 July 2013; received in revised form 6 April 2014; accepted 7 April 2014

Abstract

A phase-field model is developed to study the cubic to monoclinic martensitic phase transformation in nickel–titanium (NiTi) shape memory alloys. Three-dimensional phase-field simulations show the nucleation and growth of monoclinic B19′ multivariants that form a polytwinned martensitic microstructure. Parametric studies demonstrate that mechanical constraints and crystallographic orientation govern the patterning of martensitic twin variants in the formation of strain-accommodating microstructures. Pairing of twin variants is studied by comparing the phase-field simulation results with the crystallographic solutions of compatible twins. The phase-field method developed in this work is generally applicable to simulate the dynamic microstructure evolution of metals and alloys that produce low-symmetry phases through martensitic transformation.

Keywords: Phase-field simulation; Shape memory alloys; Polytwinned microstructure

1. Introduction

Nickel–Titanium (NiTi) is the most widely used shape memory alloy [1–4]. Its shape memory effect is primarily governed by the martensitic phase transformation between the cubic B2 (austenite) and the monoclinic B19′ phase (martensite) [5]. Understanding the mechanism of martensitic transformation in NiTi is essential to controlling and optimizing its shape memory behavior.

The martensitic phase transformation in NiTi has been studied by a variety of modeling methods. The continuum models are usually focused on the crystallography and compatibility of the phase transformation and twin microstructure [6–8]. First-principles calculations are well suited to investigating the atomic-level structures and their stabilities, as well as phase-transformation pathways [9–13]. Atomistic studies based on empirical interatomic potentials can explore the phase transformation and martensitic microstructure in systems larger than those accessible by first-principles methods [14–18]. However, both first-principles and interatomic-potential-based studies are severely limited by the spatial and temporal scales that are achievable. Such limitations can be alleviated by use of the phase-field model, which is particularly suited to studying the dynamic evolution of martensitic microstructures [19–24].

The NiTi system generally involves a variety of metastable phases (B2, B19, B19′, R, etc.), martensite variants (e.g. 12 variants in the B19′ phase) and twin structures (such as type I, II and compound twins). Such phase and structure complexities pose significant challenges to computational modeling. Nevertheless, progress has been recently made in the development of phase-field models for the NiTi system. For example, Shu and Yen developed a multivariant

* Corresponding author at: Woodruff School of Mechanical Engineering, Georgia Institute of Technology, Atlanta, GA 30332, USA.
E-mail address: ting.zhu@me.gatech.edu (T. Zhu).

http://dx.doi.org/10.1016/j.actamat.2014.04.013
1359-6454/

model to study the martensitic microstructure of the R phase [25]. Yang and Dayal proposed a simple energy function to describe the B19′ multivariants [26]. Both models assumed the penalty-based energy function and were applied to two-dimensional (2-D) phase-field simulations. However, the phase-field model with a physics-based Landau-type energy function is still not available. The Landau-type polynomial energy function is favored in the phase-field model, because it can facilitate a direct link between the model parameters and physical properties such as undercooling temperature [19] and defect energy [27]. It is, however, non-trivial to construct a Landau-type polynomial energy function to characterize the martensitic transform to low-symmetry phases. In the case of NiTi, this is due to the difficulty of representing the 13 coexisting metastable energy wells on the system energy landscape, which respectively correspond to the cubic B2 phase and 12 monoclinic B19′ variants. Meanwhile, other metastable energy wells should be eliminated to avoid the interference of physically irrelevant states. In this work, we construct an effective Landau-type polynomial energy function and perform 3-D phase-field simulations of the B2–B19′ phase transformation. The results reveal the nucleation and growth of polytwinned morphology of martensitic microstructures. The effects of mechanical constraints and crystallographic orientation on the patterning of multivariants in the formation of strain-accommodating microstructures are investigated.

2. Phase-field model

We take a single crystal of B2 austenite as the starting configuration. This parent austenitic phase can transform to B19′ martensite when the temperature is reduced below the martensite start temperature. The phase-field model provides the solutions of the temporal evolution of phases and microstructures by numerically solving the time-dependent partial differential equations of field variables. Twelve continuous field variables $\{\eta_1, \ldots, \eta_{12}\}$ between 0 and 1 are defined to describe the B2–B19′ transformation, which involves one cubic B2 phase and 12 monoclinic B19′ variants. The austenitic B2 phase corresponds to the case of $\eta_1 = \cdots = \eta_{12} = 0$. Variant i of the martensitic B19′ phase is represented by $\eta_i = 1$ and $\eta_j = 0$ for all $j \neq i$.

The stress-free strain, which arises from local phase transformation, can be described as:

$$\boldsymbol{\varepsilon}^*(\mathbf{x}) = \sum_{i=1}^{12} \eta_i(\mathbf{x})\boldsymbol{\varepsilon}_i^0, \tag{1}$$

where $\boldsymbol{\varepsilon}^*(\mathbf{x})$ is the stress-free strain at a spatial position $\mathbf{x}$, and $\boldsymbol{\varepsilon}_i^0$ is the strain of the complete transformation from B2 to B19′ for variant i.

The free energy of the system, F, can be described by the volume integral of three free energy densities, including local (chemical) energy density f_{local}, gradient energy density f_{grad}, and elastic strain energy density f_{el}:

$$F = \int_V (f_{\text{local}} + f_{\text{grad}} + f_{\text{el}})dV. \tag{2}$$

2.1. Local free energy

The local free energy density f_{local} is governed by the bulk thermodynamic properties of the system. A Landau-type polynomial is used to represent f_{local} as follows:

$$f_{\text{local}} = f_0 + \Delta f(T)\left\{\frac{1}{2}A\left(\sum_{i=1}^{12}\eta_i^2\right) - \frac{1}{3}B\left(\sum_{i=1}^{12}\eta_i^3\right) + \frac{1}{4}C\left(\sum_{i=1}^{12}\eta_i^2\right)^2 + \frac{1}{4}D\left(\sum_{i=1}^{12}\eta_i^4\right)\right\}, \tag{3}$$

where f_0 is the free energy density of the austenitic phase and can be set as zero, $\Delta f(T)$ is the difference of the free energy density between austenite and martensite that depends on temperature T, and A, B, C and D are constants characterizing the shape of the free energy density function f_{local}. Note that parameters A, B, C and D cannot be arbitrarily assigned, and three constraints must be satisfied. Firstly, the partial derivative of f_{local} with respect to the field variables $\{\eta_1, \ldots, \eta_{12}\}$ must be zero when $\eta_1 = \cdots = \eta_{12} = 0$, or $\eta_i = 1$ and $\eta_j = 0$ for all $j \neq i$, such that the austenitic and martensitic phases correspond to local energy minima. Secondly, the difference in the free energy density between austenite and martensite should be $\Delta f(T)$. These two requirements lead to:

$$\begin{cases} -A + B - C - D = 0 \\ \frac{1}{2}A - \frac{1}{3}B + \frac{1}{4}C + \frac{1}{4}D = -1 \end{cases}. \tag{4}$$

In this work we choose to represent f_{local} with the following set of parameters $A = 1$, $B = 15$, $C = 7$ and $D = 7$, which provide physically reasonable phase-field results for martensitic microstructure evolution. The driving force on each field variable η_i associated with f_{local} is given by:

$$F_i^{\text{local}} = -\frac{\partial f_{\text{local}}}{\partial \eta_i} = \Delta f(T)\left\{-A\eta_i + B\eta_i^2 - C\eta_i\left(\sum_{j=1}^{12}\eta_j^2\right) - D\eta_i^3\right\}. \tag{5}$$

Thirdly, the B2 phase should be a thermodynamically metastable state. This requirement is related to the choice of $\Delta f(T)$ and will be examined later.

2.2. Gradient energy

The gradient energy density f_{grad} is the nonlocal part of the chemical free energy density, which characterizes the energy of the interface between neighboring twin variants. We express f_{grad} in terms of the gradient of field variables:

$$f_{\text{grad}} = \frac{1}{2}\sum_{p=1}^{12}\beta_{ij}(p)\frac{\partial \eta_p}{\partial x_i}\frac{\partial \eta_p}{\partial x_j}, \tag{6}$$

where the Einstein summation convention is applied only for index i and j. In Eq. (6), the coefficients $\beta_{ij}(p)$ are the components of a semipositive definite tensor; they are not necessarily the same among different field variables η_p, and may be anisotropic depending on the direction of the gradient given by partial derivatives with respect to spatial coordinates x_i and x_j. In order to capture the essential physical effects of phase transformation and microstructure evolution with reduced numerical complexity, isotropic gradient energy is assumed in this work. Namely, we take $\beta_{ij}(p) = \beta\delta_{ij}$, where δ_{ij} is the Kronecker delta. It follows that Eq. (6) is reduced to:

$$f_{\text{grad}} = \frac{1}{2}\sum_{p=1}^{12}\beta|\nabla\eta_p|^2. \tag{7}$$

The driving force on each field variable η_i associated with f_{grad} is [25]:

$$F_i^{\text{grad}} = \beta\nabla^2\eta_i. \tag{8}$$

2.3. Elastic energy

The elastic energy density f_{el} is given by:

$$f_{\text{el}} = \frac{1}{2}(\boldsymbol{\varepsilon} - \boldsymbol{\varepsilon}^*)^{\mathrm{T}}\mathbf{C}(\boldsymbol{\varepsilon} - \boldsymbol{\varepsilon}^*), \tag{9}$$

where $\boldsymbol{\varepsilon} = (\varepsilon_{11}, \varepsilon_{22}, \varepsilon_{33}, 2\varepsilon_{23}, 2\varepsilon_{31}, 2\varepsilon_{12})^{\mathrm{T}}$ is the total strain, and $\boldsymbol{\varepsilon}^* = (\varepsilon_{11}^*, \varepsilon_{22}^*, \varepsilon_{33}^*, 2\varepsilon_{23}^*, 2\varepsilon_{31}^*, 2\varepsilon_{12}^*)^{\mathrm{T}}$ is the stress-free strain of phase transformation, and $\mathbf{C}$ is the 6×6 stiffness matrix in the Voigt notation. The constitutive equation can be derived from Eq. (9) with the stress given by:

$$\boldsymbol{\sigma} = (\sigma_{11}, \sigma_{22}, \sigma_{33}, \sigma_{23}, \sigma_{31}, \sigma_{12})^{\mathrm{T}} = \mathbf{C}(\boldsymbol{\varepsilon} - \boldsymbol{\varepsilon}^*). \tag{10}$$

The driving force acting on each field variable η_i associated with f_{el} is:

$$F_i^{\text{el}} = -\frac{\partial f_{\text{el}}}{\partial\eta_i} = [\mathbf{C}(\boldsymbol{\varepsilon} - \boldsymbol{\varepsilon}^*)]^{\mathrm{T}}\frac{\partial\boldsymbol{\varepsilon}^*}{\partial\eta_i} = \boldsymbol{\sigma}^{\mathrm{T}}\frac{\partial\boldsymbol{\varepsilon}^*}{\partial\eta_i}. \tag{11}$$

In this work, we study the boundary conditions under either applied strain and/or zero applied stress ($\boldsymbol{\sigma}^a = 0$), such that the term involving the applied traction vanishes. Both the total strain $\boldsymbol{\varepsilon}$ and stress $\boldsymbol{\sigma}$ can be solved using the technique of Fourier transform, and the detailed formulas are derived in the Appendix A.

2.4. Phase-field equation

The evolution of the phase field is governed by the time-dependent Ginzburg–Landau (TDGL) equation, which is a stochastic phase-field kinetic equation based on the assumption that the rate of change of field variables is proportional to the thermodynamic driving force:

$$\frac{\partial\eta_i}{\partial t} = \sum_{j=1}^{12}\left[\widehat{L}_{ij}\left(F_j^{\text{local}} + F_j^{\text{grad}} + F_j^{\text{el}}\right)\right] + \xi_i(\mathbf{x}, t), \tag{12}$$

where $\widehat{L}_{ij}$ is the matrix of kinetic coefficients, and $\xi_i(\mathbf{x}, t)$ is the Langevin noise term which follows the normal distribution and is mutually independent at different locations and times. To satisfy the requirement of the fluctuation–dissipation theorem [19], the correlation of $\xi_i(\mathbf{x}, t)$ is given by:

$$\langle\xi_i(\mathbf{x}, t)\xi_j(\mathbf{x}', t')\rangle = 2k_{\mathrm{B}}T\widehat{L}_{ij}\delta_{ij}\delta(\mathbf{x} - \mathbf{x}')\delta(t - t'), \tag{13}$$

where k_{B} is the Boltzmann constant and δ is the Dirac delta function. For simplicity, the kinetic coefficient $\widehat{L}_{ij}$ is assumed diagonal, i.e. $\widehat{L}_{ij} = L\delta_{ij}$, with the assumption that the driving force on each field variable η_i does not affect the evolution of field variable η_j when $i \neq j$. Substitution of Eqs. (5) and (8) into Eq. (12) yields:

$$\frac{\partial\eta_i}{\partial t} = L\left\{\Delta f(T)\left[-A\eta_i + B\eta_i^2 - C\eta_i\left(\sum_{j=1}^{12}\eta_j^2\right) - D\eta_i^3\right] + \beta\nabla^2\eta_i + F_i^{\text{el}}\right\} + \xi_i(\mathbf{x}, t). \tag{14}$$

2.5. Numerical simulation

The phase-field simulations are performed in a 3-D cubic cell, subjected to periodic boundary conditions in all three directions. We discretize the 3-D cell into uniform grids and the time into equal steps. All of the field variables at time step n are represented in the form of $\eta_i^n(x, n\Delta t)$ for $i = 1, \ldots, 12$, where Δt denotes the time step size. It is convenient to normalize the length and time scales, thereby eliminating the unnecessary parameters. We define the dimensionless space coordinate $\widetilde{x}_1 = x_1/l_0$, $\widetilde{x}_2 = x_2/l_0$ and $\widetilde{x}_3 = x_3/l_0$, where l_0 is the size of the grid cell, and the dimensionless time $\widetilde{t} = tL\Delta f(T)$ and $\Delta\widetilde{t} = \Delta tL\Delta f(T)$. It follows that Eq. (14) is normalized as:

$$\frac{\partial\eta_i}{\partial\widetilde{t}} = \left[-A\eta_i + B\eta_i^2 - C\eta_i\left(\sum_{j=1}^{12}\eta_j^2\right) - D\eta_i^3\right] + \widetilde{\beta}\widetilde{\nabla}^2\eta_i + \frac{F_i^{\text{el}}}{\Delta f(T)} + \widetilde{\xi}_i(\widetilde{\mathbf{x}}, t), \tag{15}$$

where $\widetilde{\nabla}^2 = \frac{\partial^2}{\partial\widetilde{x}_1^2} + \frac{\partial^2}{\partial\widetilde{x}_2^2} + \frac{\partial^2}{\partial\widetilde{x}_3^2}$, $\widetilde{\beta} = \frac{\beta}{\Delta f(T)l_0^2}$ and $\widetilde{\xi}_i(\widetilde{\mathbf{x}}, t) = \frac{1}{L\Delta f(T)}\xi_i(\widetilde{\mathbf{x}}, t)$. The random variable $\widetilde{\xi}_i(\widetilde{\mathbf{x}}, t)$, which is mutually independent at different space coordinates and time steps, follows the normal distribution with the mean of zero and the variance of $\frac{2k_{\mathrm{B}}T}{\Delta f(T)l_0^3}$.

To solve a partial differential equation of the heat-equation type by numerical integration, one can typically apply the forward Euler (explicit) method, the backward Euler (implicit) method or the Crank–Nicolson (implicit) method. The nonlinear terms, i.e. the first and third terms in Eq. (15), pose a computational challenge to either the backward Euler or the Crank–Nicolson method. On the other hand, the stability condition of the forward Euler method due to the Laplace operator limits the time step size $\Delta\widetilde{t} \approx \Delta\widetilde{x}^2$. To overcome these difficulties, we use the semi-implicit Fourier-spectral method proposed by Chen and Shen [21] which provides an efficient and accurate

solution for the TDGL equation. The key of this semi-implicit method is to calculate the Laplace term implicitly and the nonlinear terms explicitly, such that Eq. (15) can be discretized as:

$$\frac{\eta_i^{n+1}-\eta_i^n}{\Delta\widetilde{t}}=\left(\frac{F_i^{\text{local}}(\boldsymbol{\eta}^n(\boldsymbol{x},n\Delta\widetilde{t}))}{\Delta f(T)}+\widetilde{\beta}\widetilde{\nabla}^2\eta_i^{n+1}(\mathbf{x},(n+1)\Delta\widetilde{t})+\frac{F_i^{\text{el}}(\boldsymbol{\eta}^n(\boldsymbol{x},n\Delta\widetilde{t}))}{\Delta f(T)}\right)+\widetilde{\xi}_i(\widetilde{\mathbf{x}},(n+1)\Delta\widetilde{t}). \tag{16}$$

It is computationally efficient to solve Eq. (16) in the Fourier space, so as to avoid the inverse Fourier transformation of stress. To this end, the Laplace operator is transformed to $-4\pi(s_1^2+s_2^2+s_3^2)$ in Fourier space, where $\mathbf{s}=(s_1,s_2,s_3)^{\mathrm{T}}$ is the coordinate in Fourier space. Eq. (16) can be transformed to:

$$\widehat{\eta_i^{n+1}}=\frac{1}{1+4\pi\widetilde{\beta}(s_1^2+s_2^2+s_3^2)\Delta\widetilde{t}}\left(\widehat{\eta_i^n}+\frac{\Delta\widetilde{t}}{\Delta f(T)}\widehat{F_i^{\text{local}}(\boldsymbol{\eta}^n)}+\frac{\Delta\widetilde{t}}{\Delta f(T)}\widehat{F_i^{\text{el}}(\boldsymbol{\eta}^n)}\right) \tag{17}$$

2.6. Model parameters

In Eq. (1), the stress-free strains of the B2–B19′ transformation are described by 12 field variables $\{\eta_1,\ldots,\eta_{12}\}$ that represent 12 B19′ variants, respectively. When the global Cartesian coordinate system is aligned with the cubic axes of the parent B2 phase, the 12 transformation strain tensors $\boldsymbol{\varepsilon}_i^0$ $(i=1,\ldots,12)$ in Eq. (1) are given by:

$$\boldsymbol{\varepsilon}_1^0=\begin{pmatrix}\theta&\rho&\rho\\ \rho&\sigma&\tau\\ \rho&\tau&\sigma\end{pmatrix},\quad \boldsymbol{\varepsilon}_2^0=\begin{pmatrix}\theta&-\rho&-\rho\\ -\rho&\sigma&\tau\\ -\rho&\tau&\sigma\end{pmatrix},\quad \boldsymbol{\varepsilon}_3^0=\begin{pmatrix}\theta&-\rho&\rho\\ -\rho&\sigma&-\tau\\ \rho&-\tau&\sigma\end{pmatrix},$$
$$\boldsymbol{\varepsilon}_4^0=\begin{pmatrix}\theta&\rho&-\rho\\ \rho&\sigma&-\tau\\ -\rho&-\tau&\sigma\end{pmatrix},\quad \boldsymbol{\varepsilon}_5^0=\begin{pmatrix}\sigma&\rho&\tau\\ \rho&\theta&\rho\\ \tau&\rho&\sigma\end{pmatrix},\quad \boldsymbol{\varepsilon}_6^0=\begin{pmatrix}\sigma&-\rho&\tau\\ -\rho&\theta&-\rho\\ \tau&-\rho&\sigma\end{pmatrix},$$
$$\boldsymbol{\varepsilon}_7^0=\begin{pmatrix}\sigma&-\rho&-\tau\\ -\rho&\theta&\rho\\ -\tau&\rho&\sigma\end{pmatrix},\quad \boldsymbol{\varepsilon}_8^0=\begin{pmatrix}\sigma&\rho&-\tau\\ \rho&\theta&-\rho\\ -\tau&-\rho&\sigma\end{pmatrix},\quad \boldsymbol{\varepsilon}_9^0=\begin{pmatrix}\sigma&\tau&\rho\\ \tau&\sigma&\rho\\ \rho&\rho&\theta\end{pmatrix},$$
$$\boldsymbol{\varepsilon}_{10}^0=\begin{pmatrix}\sigma&\tau&-\rho\\ \tau&\sigma&-\rho\\ -\rho&-\rho&\theta\end{pmatrix},\quad \boldsymbol{\varepsilon}_{11}^0=\begin{pmatrix}\sigma&-\tau&\rho\\ -\tau&\sigma&-\rho\\ \rho&-\rho&\theta\end{pmatrix},$$
$$\boldsymbol{\varepsilon}_{12}^0=\begin{pmatrix}\sigma&-\tau&-\rho\\ -\tau&\sigma&\rho\\ -\rho&\rho&\theta\end{pmatrix}. \tag{18}$$

The components of $\boldsymbol{\varepsilon}_i^0$ in Eq. (18) have been calculated by Hane and Shield [7] using the lattice constants given by Otsuka et al. [5], i.e. $\theta=-0.0437$, $\sigma=0.0243$, $\rho=-0.0427$ and $\tau=0.0580$. When the global Cartesian coordinate system is not aligned with the cubic axes of the parent B2 phase, a rotation operation of $\mathbf{R}\boldsymbol{\varepsilon}_i^0\mathbf{R}^{\mathrm{T}}$ is required, where $\mathbf{R}$ is the rotation matrix.

The elastic constant matrix $\mathbf{C}$ is taken from the density functional calculations by Hatcher et al. [10], i.e. $C_{11}=183$ GPa, $C_{12}=146$ GPa and $C_{44}=46$ GPa. The typical strain energy density, which scales with $\boldsymbol{\varepsilon}_1^{0\mathrm{T}}\mathbf{C}\boldsymbol{\varepsilon}_1^0$, is $\sim 4.403\times10^8$ J m^{-3}. We take $\Delta f(T)$ to be 10% of the strain energy, i.e. $\Delta f(T)=4.403\times10^7$ J m^{-3}. A simple linear relation between $\Delta f(T)$ and the undercooling temperature ΔT is assumed [19]:

$$\Delta f(T)=Q\frac{\Delta T}{T_0}. \tag{19}$$

In Eq. (19), the latent heat is taken as $Q=110$ MJ m^{-3} and the equilibrium temperature as $T_0=271$ K [28], so that the undercooling temperature is about $\Delta T=108$ K given the above assigned value of $\Delta f(T)$.

In Section 2.1, we note that the local free energy density f_{local} should satisfy the physical requirement that the B2 phase is a thermodynamically metastable state. From Eq. (3), one obtains $\frac{\partial^2 f_{\text{local}}}{\partial\eta_i^2}=\Delta f(T)(A-2B\eta_i+3C\eta_i^2+3D\eta_i^2)$ when $\eta_j=0$ for all $j\neq i$. To represent the B2 phase, η_i has to be zero as well, such that $\left.\frac{\partial^2 f_{\text{local}}}{\partial\eta_i^2}\right|_{\eta_i=0}=\Delta f(T)A$. Since both $\Delta f(T)$ and A are taken as positive values, it follows that $\left.\frac{\partial^2 f_{\text{local}}}{\partial\eta_i^2}\right|_{\eta_i=0}>0$, thereby showing that the B2 phase is a thermodynamically metastable state in our phase-field model.

The interfacial energy density γ (i.e. interfacial energy per unit area) is related to the coefficient β in Eq. (7) according to $\gamma=\frac{4\sqrt{2}}{3}\sqrt{\beta\Delta f(T)}$ [29]. We use the normalized interfacial energy coefficient $\widetilde{\beta}$ in Eq. (15). It follows that the grid size becomes $l_0=\frac{3\gamma}{4\Delta f(T)\sqrt{2\widetilde{\beta}}}$, where γ is taken as the interfacial energy density of type I twin, 187 mJ m^{-2} [13].

The time step needs to be carefully chosen to ensure the convergence of numerical integration. By trial and error, we find that $\Delta\widetilde{t}=0.01$ provides reasonable accuracy and efficiency. The numerical integration is performed up to 12,500 time steps (i.e. $\widetilde{t}=125$), and selected simulations with longer times show no further change in the microstructures.

3. Results and discussion

3.1. Microstructure evolution

To study the nucleation and growth of martensitic microstructures, we first conduct a phase-field simulation under a mixed loading condition: zero in-plane strain and zero out-of-plane stress, i.e. $\varepsilon_1^a=\varepsilon_2^a=\varepsilon_6^a=0$ and $\sigma_3^a=\sigma_4^a=\sigma_5^a=0$. Such boundary conditions correspond to a thin film subjected to rigid constraints from the substrate. The global Cartesian coordinate system is aligned with the cubic axes of the parent B2 phase, as shown in Fig. 1. The system contains $64\times64\times64$ mesh grids. We set $\widetilde{\beta}=2$, so that $l_0=\frac{3\gamma}{4\Delta f(T)\sqrt{2\widetilde{\beta}}}=1.6$ nm and accordingly the simulation cell has a side length of $\sim$102.4 nm.

Given the positive value of $\Delta f(T)$, the martensitic transformation of B2→B19′ is energetically favored. However,

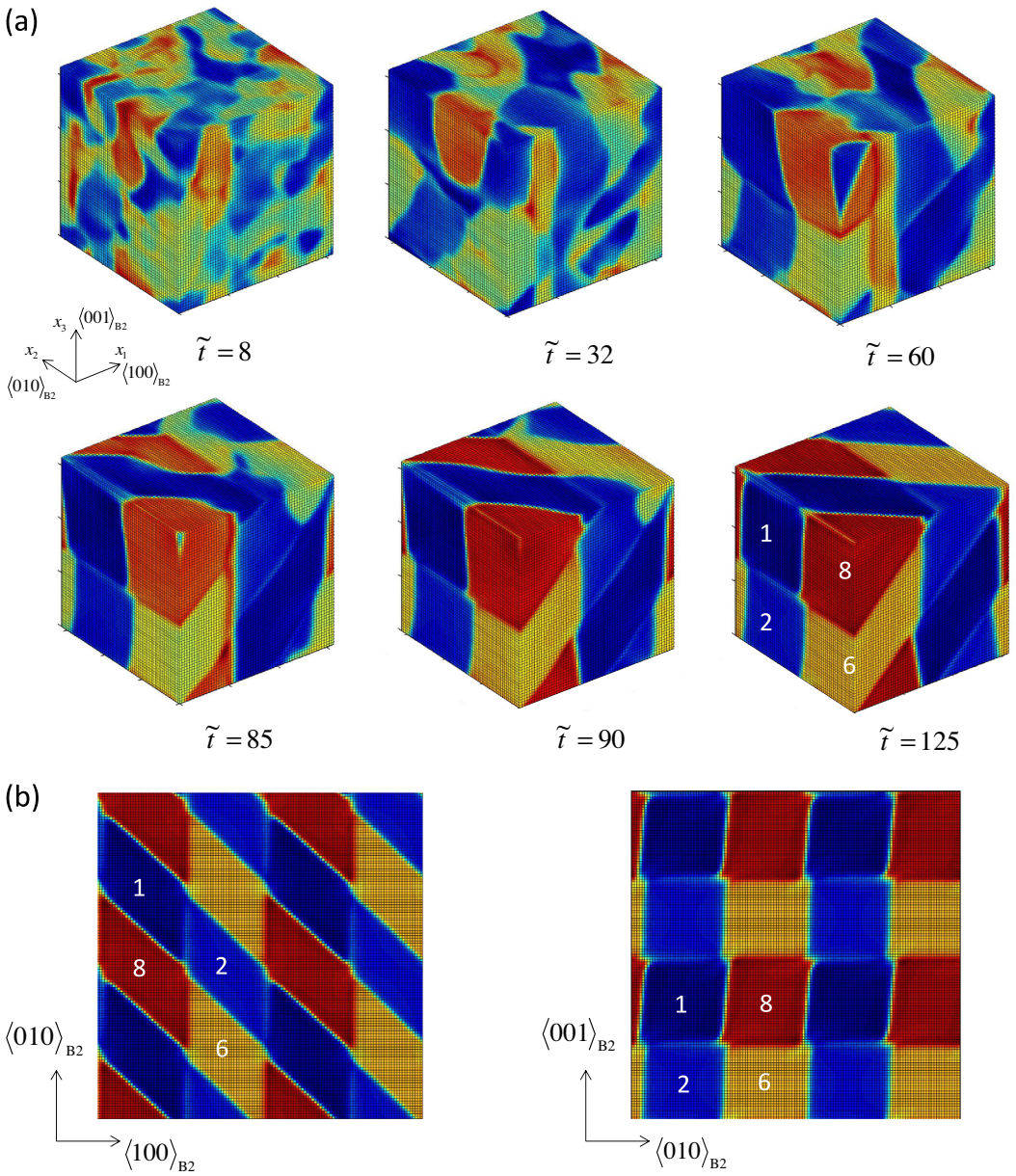

Fig. 1. A 3-D phase-field simulation result of martensitic transformation from B2 to B19′, showing the formation of polytwinned microstructure. (a) Time-lapse snapshots showing the nucleation and growth of twinned B19′ structures. The mesh grids are colored by the value of $\sum_{i=1}^{12} i\eta_i(x)$, showing different twin variants. (b) 2-D projections of the 3-D microstructure at $\tilde{t} = 125$. The actual simulation cell, as shown in (a), is periodically doubled in the two in-plane directions in (b), in order to provide a clear visualization of the polytwinned structure. (For interpretation of the references to colour in this figure legend, the reader is referred to the web version of this article.)

owing to the metastable state of the B2 phase, the martensitic transformation would not occur spontaneously, thus requiring thermal fluctuations to assist the nucleation of martensite. The Langevin noise term $\xi_i(\mathbf{x}, t)$ in Eq. (12) plays a role in thermal fluctuations. This stochastic term is independent of each other at different time steps or spatial locations, and thus does not provide any constraint on the phase-transformation process. It is turned off after 3000 simulation steps when $\tilde{t} = 30$.

Fig. 1a shows the nucleation and growth of martensite, resulting in a polytwinned microstructure. At $\tilde{t} = 8$, the martensite precursors form, driven by the positive Δf and facilitated by thermal fluctuations. Colors represent different values of field variables η_i. Appearance of multiple colors indicates the nucleation of multivariants. At this stage, none of the field variables η_i is close to 1 and thus no B19′ variant is fully formed. However, the field variables also deviate from all-zero values (the metastable B2 phase). These martensite precursors cause lattice distortion, as evidenced by the increase of local elastic energy. They form and disappear during this early stage. The microstructure further evolves from the existing lattice distortion promoted by thermal fluctuations, when the stochastic noise terms are turned off at $\tilde{t} = 30$. At $\tilde{t} = 32$, shortly after

the turn-off of stochastic noise terms, nuclei with sizes around tens of nanometers are generated. The boundaries of nuclei are curved and no obvious laminate twin structure is visible. The growth and elimination of these nuclei are driven by the dynamic changes of local free energy, gradient energy and elastic energy that collectively lower the total energy of the system. The laminate twin pattern first emerges at $\tilde{t} = 60$, when several nuclei, colored red, blue and green, grow into different twin variants. Other nuclei disappear at $\tilde{t} = 85$. Soon after, the twin pattern becomes stable at $\tilde{t} = 90$, while the twin boundaries are still not flat. Finally, at $\tilde{t} = 125$, the 3-D twin microstructure consisting of four different B19′ variants forms with the respective transformation strain of $\boldsymbol{\varepsilon}_1^0, \boldsymbol{\varepsilon}_2^0, \boldsymbol{\varepsilon}_6^0$ and $\boldsymbol{\varepsilon}_8^0$. Fig. 1b shows the top and left-side view of the 3-D polytwinned microstructure at $\tilde{t} = 125$.

Given the above polytwinned microstructure, it is necessary to examine whether the multivariants are geometrically compatible with the prescribed boundary condition, as well as satisfy the geometric compatibility at each individual twin boundary. From a consideration of the energetics, the transformation from austenite to martensite lowers the local (chemical) energy. Regarding the strain energy, we note that the total strain $\boldsymbol{\varepsilon}$, transformation strain $\boldsymbol{\varepsilon}^*$ and stress $\boldsymbol{\sigma}$ can be decomposed into the homogeneous and inhomogeneous components, as defined in the Appendix A. It follows that the homogeneous part of the strain energy can be minimized by adjusting the volume fractions of multivariants to accommodate the applied boundary condition. On the other hand, the nucleated martensite variants form twins, such that the heterogeneous part of the strain energy can be minimized if the compatibility requirements are fully satisfied at twin boundaries. To check the compatibility with the prescribed boundary condition in phase-field simulations, we estimate the average transformation strain of the final state at $\tilde{t} = 125$ by assuming equal volume fractions of the four variants:

$$(\boldsymbol{\varepsilon}_1^0 + \boldsymbol{\varepsilon}_2^0 + \boldsymbol{\varepsilon}_6^0 + \boldsymbol{\varepsilon}_8^0)/4 = \begin{pmatrix} -0.01 & 0 & 0 \\ 0 & -0.01 & 0.0504 \\ 0 & 0.0504 & 0.0243 \end{pmatrix}. \tag{20}$$

Eq. (20) indicates that each in-plane component of the average transformation strain is small with ~1% compressive normal strain and zero shear strain, and thus satisfies approximately the applied boundary condition of zero in-plane strain: $\varepsilon_1^a = \varepsilon_2^a = \varepsilon_6^a = 0$.

We next examine the geometrical compatibility of variants at twin boundaries by comparing the phase-field results with the theoretical crystallographic solutions tabulated by Hane and Shield [7]. In Fig. 1 the observed twin planes between each pair of variants {2:6}, {1:8}, {1:2} and {6:8} are all of the {1 1 0} type, as summarized in Table 1. Three of the four pairs are consistent with the crystallographic solutions of type I twin in NiTi, except the {6:8} pair whose violation of compatibility at the twin interface increases the heterogeneous strain energy. However, the emergence of such an incompatible twin pair is geometrically necessary for accommodating the other three twin pairs, so as to reduce the overall energy of the system. Generally, theoretical solutions based on the principle of geometric compatibility at twin interfaces [7] provide a guide for selecting twin pairs when the applied stress is zero. However, under the boundary conditions such as applied strain/displacement, there might be no "perfect" solution which is fully compatible at all the twin interfaces and hence minimizes the local (chemical) free energy and the homogeneous and heterogeneous strain energies simultaneously. In other words, the compatibility condition is not always guaranteed at every twin interface in realistic microstructures [5], as shown in our phase-field simulations.

Table 1
Pairing of twin variants from crystallography theory and the phase-field simulation in Fig. 1.

Twin pair	Theoretical solution [7]	Phase field
{2:6}	{1 1 0} type I	{1 1 0}
{1:8}	{1 1 0} type I	{1 1 0}
{1:2}	{1 1 0} compound	{1 1 0}
{6:8}	{1 0 0} type I	{1 1 0}

The martensitic phase transformation in a complex system such as NiTi could yield a non-unique final product. We repeat the phase-field simulation with all the parameters unchanged to explore different possible microstructures. Different polytwinned structures arise due to the stochastic effect of the Langevin noise term $\xi_i(\mathbf{x}, t)$ in Eq. (12). Fig. 2a shows another phase-field simulation result of martensite nucleation and microstructure evolution, which contrasts with those in Fig. 1a. As seen from Fig. 2a, the precursors of martensite initially form and disappear at $\tilde{t} = 20$, similar to Fig. 1a. At $\tilde{t} = 50$, martensitic nuclei form and merge with others containing the same type of twin variant, and finally form a polytwinned structure at $\tilde{t} = 125$. This final state consists of four different B19′ variants with the basis transformation strain $\boldsymbol{\varepsilon}_2^0, \boldsymbol{\varepsilon}_4^0, \boldsymbol{\varepsilon}_5^0$ and $\boldsymbol{\varepsilon}_6^0$, respectively. In this case, the twin interfaces are parallel to the side faces of the simulation cell, in contrast to the inclined ones in Fig. 1a. The top view of the 3-D polytwinned structure is shown in Fig. 2b. For the {2:6} and {4:5} pairs, their twin planes are of the {1 1 0} type, while the other two pairs have twin planes of the {1 0 0} type, as summarized in Table 2. Similar to the result in Fig. 1, compatibility is not satisfied for the {5:6} pair, while the other three pairs are geometrically compatible at the respective twin interface. Likewise, the average transformation strain of variants 2, 4, 5 and 6 at $\tilde{t} = 125$ is estimated by assuming the equal volume fractions of four variants:

$$(\boldsymbol{\varepsilon}_2^0 + \boldsymbol{\varepsilon}_4^0 + \boldsymbol{\varepsilon}_5^0 + \boldsymbol{\varepsilon}_6^0)/4 = \begin{pmatrix} -0.01 & 0 & 0.0504 \\ 0 & -0.01 & 0 \\ 0.0504 & 0 & 0.0243 \end{pmatrix}. \tag{21}$$

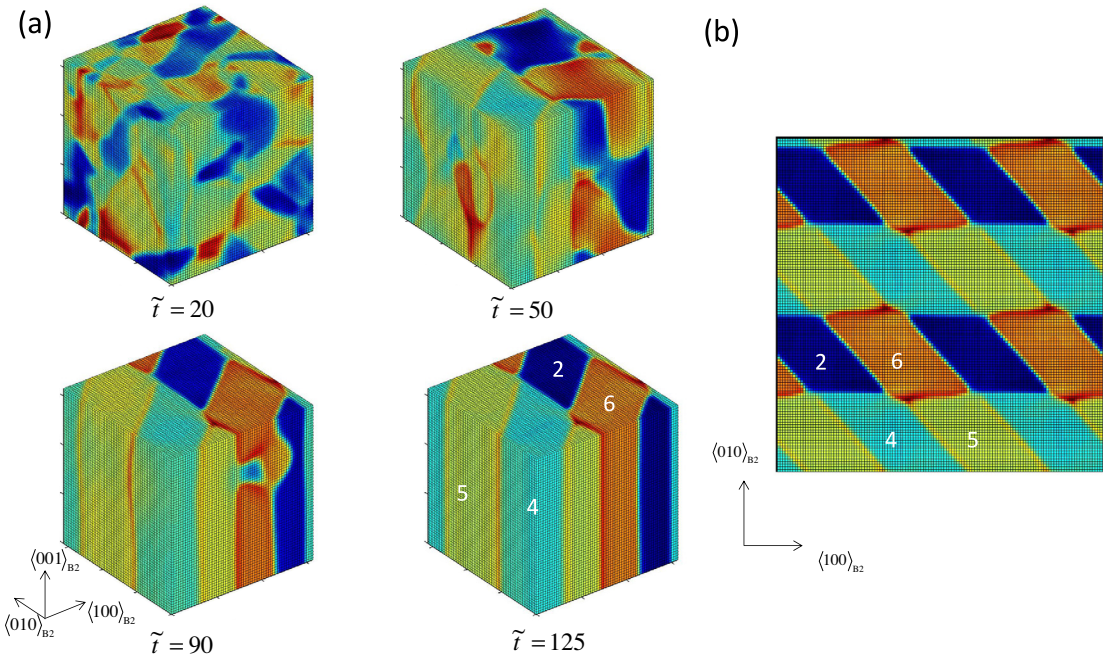

Fig. 2. A different phase-field simulation result of polytwinned microstructure under the same boundary condition as Fig. 1. (a) Time-lapse snapshots showing the nucleation and growth of twinned martensite. (b) 2-D projection of the 3-D microstructure at $\tilde{t}=125$. The same schemes of coloring and 2-D periodic doubling are used as in Fig. 1. (For interpretation of the references to colour in this figure legend, the reader is referred to the web version of this article.)

Table 2
Pairing of twin variants from crystallography theory and the phase-field simulation in Fig. 2.

Pair	Theoretical solution [7]	Phase field
{2:4}	{100} type I	{100}
{2:6}	{110} type I	{110}
{4:5}	{110} type I	{110}
{5:6}	{110} compound	{100}

Eq. (21) indicates that each in-plane component of the average transformation strain is small with ~1% compressive normal strain and zero shear strain, and thus approximately satisfies the applied boundary condition of zero in-plane strain $\varepsilon_1^a=\varepsilon_2^a=\varepsilon_6^a=0$.

It is interesting to note that repeated simulations with the same applied boundary condition always result in the selection of four variants from the candidate variants 1–8, but not 9–12. This is because the in-plane transformation strains among variants 1–8 can render one tensile and one compressive component, as shown in Eq. (18); they cancel each other to reduce the averaged in-plane transformation strain, so as to lower the strain energy, as shown by Eqs. (20) and (21).

3.2. Loading effect

The mechanical loading dictates the patterning of multi-variants in the formation of strain-accommodating microstructures. We next explore different combinations of boundary constraint. Here the cubic simulation cell contains $32\times32\times32$ mesh grids, $\tilde{\beta}$ is adjusted to be 0.5 and $l_0=\frac{3\gamma}{4\Delta f(T)\sqrt{2\beta}}=3.2$ nm. Correspondingly, the side length of the cell is 102.4 nm.

Fig. 3a and b show two possible microstructures when the in-plane biaxial tensile strain is applied, i.e. $\varepsilon_1^a=\varepsilon_2^a=1\%$, $\varepsilon_6^a=0$ and $\sigma_3^a=\sigma_4^a=\sigma_5^a=0$. In Fig. 3a, variants 9 and 12 form the {100} twin; in Fig. 3b, variants 10 and 11 form the {110} twin, as listed in Table 3. The transformation strain tensors associated with variants 9, 10, 11 and 12 belong to the group that shares the same normal components, but involves both in-plane tension and out-of-plane compression, as shown in Eq. (18). This group of transformation strain tensors can better match the imposed biaxial tensile strain. Pairing of variants in this group yields the self-accommodating twin structures through a complete cancellation of in-plane shear strains. Repeated simulations invariably select the variants in the group containing variants 9, 10, 11 and 12. In most cases, twin compatibility is satisfied through, for example, formation of the {100} twin between variants 9 and 12, as shown in Fig. 3a. However, exceptions are observed, such as the {110} twin of variants 10 and 11, as shown in Fig. 3b and Table 3. Selection of these twin pairs can also be understood in terms of the accommodation of the applied boundary condition, as discussed earlier. Recall that when the zero in-plane strain is applied in Section 3.1, only variants 1–8 can nucleate because the in-plane normal strain components contain both tension and compression. We also perform simulations when the in-plane biaxial

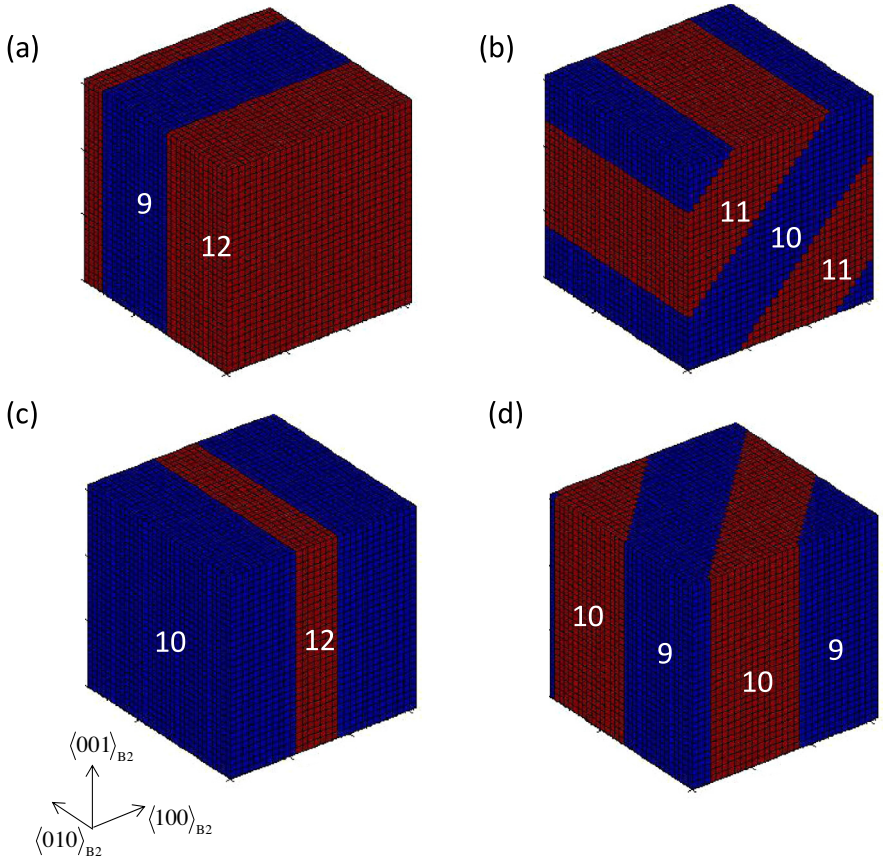

Fig. 3. Formation of polytwinned martensitic microstructures under different applied boundary conditions. The mesh is colored to distinguish different B19′ variants. (a and b) Two different microstructures form under in-plane biaxial tension $\varepsilon_1^a = \varepsilon_2^a = 1\%$, $\varepsilon_6^a = 0$ and $\sigma_3^a = \sigma_4^a = \sigma_5^a = 0$. (c and d) Two different microstructures form under out-of-plane compression $\varepsilon_3^a = -2\%$ and $\sigma_1^a = \sigma_2^a = \sigma_4^a = \sigma_5^a = \sigma_6^a = 0$. (For interpretation of the references to colour in this figure legend, the reader is referred to the web version of this article.)

Table 3
Pairing of twin variants from crystallography theory and the phase-field simulation in Fig. 3.

Twin pair	Theoretical solution [7]	Phase field
{9:12} Fig. 3a	{100} type I	{100}
{10:11} Fig. 3b	{100} type I	{110}
{10:12} Fig. 3c	{100} type I	{100}
{9:10} Fig. 3d	{110} compound	{110}

compression is applied. The resulting microstructures are identical to those in Figs. 1 and 2. These results can be similarly understood by the requirement to accommodate the imposed boundary condition.

Fig. 3c and d show the phase-field result when the out-of-plane compressive strains are applied, i.e. $\varepsilon_3^a = -2\%$ and $\sigma_1^a = \sigma_2^a = \sigma_4^a = \sigma_5^a = \sigma_6^a = 0$. Such loading mode of out-of-plane compression yields the results similar to those under in-plane biaxial tension as shown in Fig. 3a and b. This is because the two loading modes essentially differ by a hydrostatic stress that plays a minor role in the selection of twin variants. As a result, the same group containing variants 9, 10, 11 and 12 is the optimal choice, producing the {100} twin between variants 10 and 12, and the {110} twin between variants 9 and 10, as listed in Table 3.

3.3. Orientation effect

In this section, we study the orientation effects on the formation of polytwinned martensitic microstructures. In the example plotted in Fig. 4, the global Cartesian coordinate system is aligned with the ⟨110⟩, ⟨001⟩ and ⟨1$\bar{1}$0⟩ directions of the parent B2 phase. In this case, the rotation of the transformation strain tensor $\mathbf{R}\boldsymbol{\varepsilon}_i^0\mathbf{R}^{\mathrm{T}}$ is required with the rotation matrix given by:

$$\mathbf{R} = \begin{bmatrix} 0.707 & 0.707 & 0 \\ 0 & 0 & 1 \\ 0.707 & -0.707 & 0 \end{bmatrix}. \tag{22}$$

In addition, the elastic modulus tensor given in the cubic crystal system should be transformed to the global coordinate system by rotation [27] and then cast into the 6×6 stiffness matrix $\mathbf{C}$ in the Voigt notation.

Fig. 4a1 shows the simulated polytwinned microstructure under an in-plane biaxial compressive strain of 0.5%; the system is stress free in the vertical direction. The {110} twin between variants 11 and 12 is formed. Variants 11 and 12 cancel the shear transformation strain of each other, and also provide the in-plane transformation strain

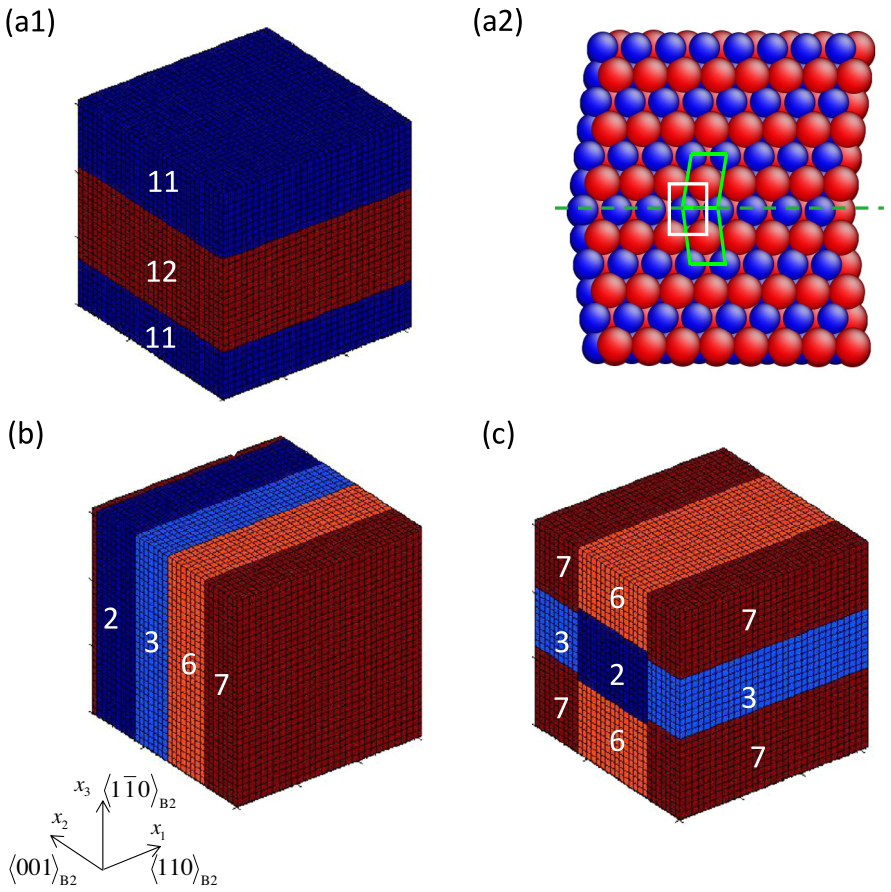

Fig. 4. Formation of polytwinned martensitic microstructures under different applied boundary conditions. (a1) {1 1 0} compound twin forms under an in-plane biaxial compressive strain of 0.5% and the system is stress free in the vertical direction. (a2) Atomic structures of {1 1 0} compound twin from a previous molecular statics simulation [16]. The green unit cells of Ni atoms (blue) exhibit tilting of the monoclinic phase, and obey the mirror-reflection condition with respect to the twin boundary (dashed line). In contrast, the white unit cell of Ti atoms (red) straddles the twin plane and retains a rectangular shape. (b) Layered twin lamellae form under an in-plane biaxial tensile strain of 1% and the system is stress free in the vertical direction. (c) Polytwinned structures form under a compressive strain of 2% in the vertical direction; all other stress components are zero. (For interpretation of the references to colour in this figure legend, the reader is referred to the web version of this article.)

of biaxial compression, thus accommodating the imposed mechanical load. The {1 1 0} twin between variants 11 and 12 is the so-called compound twin [7], as the crystallographic directions of both the twin plane and twin shear are rational.

Previously, we have conducted the interatomic-potential-based molecular statics and dynamics simulations to study the structure of compound twins [16]. Fig. 4a2 shows an example of the atomic configuration of a compound twin in a supercell under periodic boundary conditions. It is the same type of compound twin as the one in Fig. 4a1, with the twin boundary aligned with the $\{1\,1\,0\}_{B2}$ plane in the B2 basis, which corresponds to the equivalent $\{0\,1\,0\}_{B19}$ plane in the B19 basis. This atomistic study complements the continuum phase-field simulation by providing atomic-level structural details of the twin boundary. For example, Fig. 4a2 shows that the twin boundary is atomically sharp, and the mirror reflection of atoms at the twin boundary can be clearly resolved to compare with high-resolution transmission electron microscopy images, as described in detail in Ref. [16]. Furthermore, from the standpoint of multiscale modeling, one can link the atomistic and continuum phase-field simulations. For example, the atomic-level geometry such as the thickness of the atomically sharp phase boundary as revealed in Fig. 4a2, in conjunction with the atomistically calculated twin boundary energy, can provide a quantitative calibration of the gradient coefficients in the phase-field model, i.e. β_{ij} in Eq. (6). Such an atomistically informed phase-field approach is beyond the scope of this work, but warrants further study in future.

To demonstrate the loading effect, Fig. 4b shows the simulated polytwinned microstructure under an in-plane biaxial tensile strain of 1%; the system is stress free in the vertical direction. Variants 2, 3, 6 and 7 form {1 0 0} twins. The corresponding twin pairs are listed in Table 4. Selection of variants 2, 3, 6 and 7 is still dictated by the applied biaxial tension, because they are the only four variants whose in-plane components of transformation strain tensors $\mathbf{R}\boldsymbol{\varepsilon}_i^0\mathbf{R}^T$ render the biaxial elongation. Moreover, the shear component of the average transformation strain is also minimized:

Table 4
Pairing of twin variants from crystallography theory and the phase-field simulation of biaxial tension in Fig. 4b.

Twin pair	Theoretical solution [7]	Phase field
{2:3}	{100} type I	{100}
{3:6}	{110} type I	{100}
{6:7}	{100} type I	{100}
{7:2}	{110} type I	{100}

Table 5
Pairing of twin variants from crystallography theory and the phase-field simulation of biaxial tension in Fig. 4c.

Twin pair	Theoretical solution [7]	Phase field
{2:3}	{100} type I	{100}
{2:6}	{110} type I	{110}
{3:7}	{110} type I	{110}
{6:7}	{100} type I	{100}

$$\mathbf{R}(\boldsymbol{\varepsilon}_2^0+\boldsymbol{\varepsilon}_3^0+\boldsymbol{\varepsilon}_6^0+\boldsymbol{\varepsilon}_7^0)\mathbf{R}^{\mathrm{T}}/4=\begin{pmatrix}0.033 & 0 & 0\\ 0 & 0.0243 & 0\\ 0 & 0 & -0.0524\end{pmatrix}. \tag{23}$$

In addition, Fig. 4c shows the polytwinned microstructure formed when the applied compressive strain is 2% in the vertical direction and all other stress components are zero. Similarly, variants 2, 3, 6 and 7 form, although the polytwinned structure is different from the one in Fig. 4b. As summarized in Table 5, variant pairs {2:3} and {6:7} form the {1 0 0} twin; while {2:6} and {3:7} form the {1 1 0} twin. All the compatibility requirements at the twin boundary are satisfied.

4. Conclusion

We have developed a phase-field model to study the diffusionless cubic to monoclinic martensitic phase transformation in NiTi shape memory alloys. A Landau-type free energy function is constructed to characterize the martensitic transformation from the cubic B2 phase to a low-symmetry phase of monoclinic B19′ with 12 variants. 3-D phase-field simulations reveal the nucleation and growth of B19′ multivariants that form the polytwinned microstructures. The simulation results are analyzed in terms of the overall accommodation of applied boundary conditions, which reduces the homogeneous strain energy, as well as the local twin compatibility, which lowers the heterogeneous strain energy. In particular, our simulations demonstrate the difficulty of attaining the "perfect" polytwinned microstructure where the theoretical crystallographic solution of twin compatibility is satisfied ideally at every twin boundary. Further parametric studies of the loading and orientation effects show the versatility/non-uniqueness of the formation of polytwinned microstructures, where the patterning of martensitic multivariants can be interpreted in terms of the need to accommodate the applied strain. The present phase-field model provides a flexible framework to study the dynamic microstructure evolution during the martensitic transformation to low-symmetry phases.

Acknowledgement

Support by NSF Grant CMMI-0825435 is greatly acknowledged.

Appendix A. Solving strain and stress in the Fourier space

One can solve the total strain $\boldsymbol{\varepsilon}$ and stress $\boldsymbol{\sigma}$ through the Fourier transform of the equilibrium equation. To this end, we define a differential operator [25]:

$$\mathbf{A}=\begin{pmatrix}\frac{\partial}{\partial x_1} & 0 & 0 & 0 & \frac{\partial}{\partial x_3} & \frac{\partial}{\partial x_2}\\ 0 & \frac{\partial}{\partial x_2} & 0 & \frac{\partial}{\partial x_3} & 0 & \frac{\partial}{\partial x_1}\\ 0 & 0 & \frac{\partial}{\partial x_3} & \frac{\partial}{\partial x_2} & \frac{\partial}{\partial x_1} & 0\end{pmatrix}^{\mathrm{T}}, \tag{A1}$$

where x_1, x_2 and x_3 are the spatial coordinate. The geometric equation of strain can then be represented as:

$$\boldsymbol{\varepsilon}=\mathbf{A}\mathbf{u}, \tag{A2}$$

where the displacement vector is $\mathbf{u}=(u_1,u_2,u_3)^{\mathrm{T}}$ and each of its component is a function of x_1, x_2 and x_3. It follows that the equilibrium equation can be written as:

$$\mathbf{A}^{\mathrm{T}}\boldsymbol{\sigma}=\mathbf{0}. \tag{A3}$$

It is non-trivial to obtain the analytical solution of Eqs. (10), (A2), and (A3) for generally prescribed boundary conditions. Instead, these equations can be discretized and solved numerically. Direct numerical solution of Eqs. (10), (A2), and (A3) is computationally inefficient, since a set of partial difference equations for the whole field needs to be satisfied at each time step. However, for the problem with periodic boundary conditions, the semi-implicit algorithm originally developed by Chen and Shen [21] can significantly improve the computational efficiency by applying fast Fourier transformation (FFT). In this scheme, the differential equations are transformed to mutually independent linear equations at different mesh nodes. In this Appendix A, we present the detailed formulation and procedure of solving the equilibrium equations with the FFT method by partially following the approach introduced by Shu and Yen [25].

The total strain $\boldsymbol{\varepsilon}$, transformation strain $\boldsymbol{\varepsilon}^*$ and stress $\boldsymbol{\sigma}$ are decomposed into homogeneous and inhomogeneous components:

$$\boldsymbol{\varepsilon}=\langle\boldsymbol{\varepsilon}\rangle+\boldsymbol{\varepsilon}',\quad \text{where } \langle\boldsymbol{\varepsilon}\rangle=\int_V\boldsymbol{\varepsilon}\,\mathrm{d}V \tag{A4}$$

and

$$\boldsymbol{\varepsilon}^*=\langle\boldsymbol{\varepsilon}^*\rangle+\boldsymbol{\varepsilon}^{*\prime},\quad \text{where } \langle\boldsymbol{\varepsilon}^*\rangle=\int_V\boldsymbol{\varepsilon}^*\,\mathrm{d}V. \tag{A5}$$

One can further decompose the total displacement $\mathbf{u}$ into homogeneous and inhomogeneous components:

$$\mathbf{u} = \langle \mathbf{u} \rangle + \mathbf{u}' \quad \text{satisfying } \langle \boldsymbol{\varepsilon} \rangle = \mathbf{A}\langle \mathbf{u} \rangle \text{ and } \boldsymbol{\varepsilon}' = \mathbf{A}\mathbf{u}'. \tag{A6}$$

Note that the homogeneous component $\langle \mathbf{u} \rangle$ is a linear function of $\mathbf{x}$ because the homogeneous strain $\langle \boldsymbol{\varepsilon} \rangle$ is a constant. Although the decomposition in Eq. (A6) is not unique with a constant plus a rigid body rotation, it will not affect the result in which we are interested because we will only use the differential form of displacement $\mathbf{u}'$.

Substitution of Eqs. (A4) and (A5) into Eq. (10) yields:

$$\begin{aligned} \boldsymbol{\sigma} &= \mathbf{C}(\boldsymbol{\varepsilon} - \boldsymbol{\varepsilon}^*) = \mathbf{C}(\langle \boldsymbol{\varepsilon} \rangle - \langle \boldsymbol{\varepsilon}^* \rangle) + \mathbf{C}(\boldsymbol{\varepsilon}' - \boldsymbol{\varepsilon}^{*\prime}) \\ &= \langle \boldsymbol{\sigma} \rangle + \boldsymbol{\sigma}', \end{aligned} \tag{A7}$$

where the homogeneous stress is defined as:

$$\langle \boldsymbol{\sigma} \rangle = \mathbf{C}(\langle \boldsymbol{\varepsilon} \rangle - \langle \boldsymbol{\varepsilon}^* \rangle) \tag{A8}$$

and the inhomogeneous stress is:

$$\boldsymbol{\sigma}' = \mathbf{C}(\boldsymbol{\varepsilon}' - \boldsymbol{\varepsilon}^{*\prime}). \tag{A9}$$

In each simulation time step, once the field variables $\{\eta_1, \ldots, \eta_{12}\}$ are known, $\boldsymbol{\varepsilon}^*$ can be directly calculated from Eq. (1), so that it is straightforward to calculate $\langle \boldsymbol{\varepsilon}^* \rangle$ from Eq. (A5). The applied boundary conditions can be given by either $\langle \boldsymbol{\varepsilon} \rangle = \boldsymbol{\varepsilon}^a$ or $\langle \boldsymbol{\sigma} \rangle = \boldsymbol{\sigma}^a$, or a mixed type. Together with Eq. (A8), all the homogeneous components $\langle \boldsymbol{\varepsilon} \rangle$ and $\langle \boldsymbol{\sigma} \rangle$ can be obtained.

The equilibrium equation of $\boldsymbol{\sigma}'$ remains the same form:

$$\mathbf{A}^{\mathrm{T}}\boldsymbol{\sigma}' = \mathbf{0}. \tag{A10}$$

Substituting Eq. (A6) into Eqs. (A9) and (A10), we obtain the partial differential equations:

$$\mathbf{A}^{\mathrm{T}}\mathbf{C}\mathbf{A}\mathbf{u}' = \mathbf{A}^{\mathrm{T}}\mathbf{C}\boldsymbol{\varepsilon}^{*\prime}. \tag{A11}$$

For an integral equation $f: R^3 \to R$, the Fourier transformation is defined by:

$$\widehat{f(\mathbf{s})} = \mathfrak{J}(f) = \int\int\int_{-\infty}^{\infty} f(\mathbf{x}) e^{-2\pi i \mathbf{x}\cdot\mathbf{s}} d\mathbf{x}, \tag{A12}$$

where $\mathbf{s} = (s_1, s_2, s_3)^T$ is the coordinate in reciprocal space.

The inverse Fourier transformation is defined by:

$$f(\mathbf{x}) = \mathfrak{J}^{-1}(\hat{f}) = \int\int\int_{-\infty}^{\infty} \widehat{f(\mathbf{s})} e^{2\pi i \mathbf{x}\cdot\mathbf{s}} d\mathbf{s}. \tag{A13}$$

It can be shown that the differential operator $\mathbf{A}$ in real space is transformed to the linear operator $\mathbf{B}$ in reciprocal space, which is given by:

$$\mathbf{B} = 2\pi i \begin{pmatrix} s_1 & 0 & 0 & 0 & s_3 & s_2 \\ 0 & s_2 & 0 & s_3 & 0 & s_1 \\ 0 & 0 & s_3 & s_2 & s_1 & 0 \end{pmatrix}^{\mathrm{T}}. \tag{A14}$$

Then $\hat{\mathbf{u}}'$ is obtained from Eq. (A11) as:

$$\widehat{\mathbf{u}'} = \mathfrak{J}(\mathbf{u}') = (\mathbf{B}^{\mathrm{T}}\mathbf{C}\mathbf{B})^{-1}\mathbf{B}^{\mathrm{T}}\mathbf{C}\widehat{\boldsymbol{\varepsilon}^{*\prime}}. \tag{A15}$$

From Eq. (A6), the transformed inhomogeneous strain is:

$$\widehat{\boldsymbol{\varepsilon}'} = \mathfrak{J}(\boldsymbol{\varepsilon}') = \mathbf{B}(\mathbf{B}^{\mathrm{T}}\mathbf{C}\mathbf{B})^{-1}\mathbf{B}^{\mathrm{T}}\mathbf{C}\widehat{\boldsymbol{\varepsilon}^{*\prime}}. \tag{A16}$$

From Eq. (A9), the transformed inhomogeneous stress is:

$$\widehat{\boldsymbol{\sigma}'} = \mathfrak{J}(\boldsymbol{\sigma}') = \mathbf{C}\mathbf{B}(\mathbf{B}^{\mathrm{T}}\mathbf{C}\mathbf{B})^{-1}\mathbf{B}^{\mathrm{T}}\mathbf{C}\widehat{\boldsymbol{\varepsilon}^{*\prime}} - \mathbf{C}\widehat{\boldsymbol{\varepsilon}'}. \tag{A17}$$

The inhomogeneous stress and strain can be obtained by the inverse Fourier transformation according to Eq. (A13). Finally, together with the homogeneous stress given by Eq. (A8) and the boundary condition, one can obtain the driving force associated with elastic energy density given in Eq. (11). If the kinetic equations in Eq. (16) are also solved in the Fourier space, the inverse transformation of stress is not needed in the phase-field simulation.

References

[1] Christian JW, Mahajan S. Prog Mater Sci 1995;39:1.
[2] Otsuka K, Kakeshita T. MRS Bull 2002;27:91.
[3] Otsuka K, Wayman C, editors. Shape memory materials. Cambridge: Cambridge University Press; 1998.
[4] Zhu T, Li J. Prog Mater Sci 2010;55:710.
[5] Otsuka K, Ren X. Prog Mater Sci 2005;50:511.
[6] Bhattacharya K. Microstructure of martensite. In: Why it forms and how it gives rise to the shape-memory effect. Oxford: Oxford University Press; 2003.
[7] Hane KF, Shield TW. Acta Mater 1999;47:2603.
[8] Knowles KM, Smith DA. Acta Metall 1981;29:101.
[9] Hatcher N, Kontsevoi OY, Freeman AJ. Phys Rev B 2009;79:020202.
[10] Hatcher N, Kontsevoi OY, Freeman AJ. Phys Rev B 2009;80:144203.
[11] Huang XY, Ackland GJ, Rabe KM. Nat Mater 2003;2:307.
[12] Wagner MFX, Windl W. Acta Mater 2008;56:6232.
[13] Waitz T, Spisak D, Hafner J, Karnthaler HP. Europhys Lett 2005;71:98.
[14] Mutter D, Nielaba P. Phys Rev B 2010;82:224201.
[15] Mutter D, Nielaba P. Eur Phys J B 2011;84:109.
[16] Zhong Y, Gall K, Zhu T. J Appl Phys 2011;110:033532.
[17] Zhong Y, Gall K, Zhu T. Acta Mater 2012;60:6301.
[18] Zhong Y, Zhu T. Scr Mater 2012;67:883.
[19] Artemev A, Jin Y, Khachaturyan AG. Acta Mater 2001;49:1165.
[20] Chen LQ. Annu Rev Mater Res 2002;32:113.
[21] Chen LQ, Shen J. Comput Phys Commun 1998;108:147.
[22] Wang Y, Khachaturyan AG. Acta Mater 1997;45:759.
[23] Wang YZ, Li J. Acta Mater 2010;58:1212.
[24] Li LJ, Lei CH, Shu YC, Li JY. Acta Mater 2011;59:2648.
[25] Shu YC, Yen JH. Acta Mater 2008;56:3969.
[26] Yang L, Dayal K. Appl Phys Lett 2010;96:081916.
[27] Heo TW, Wang Y, Bhattacharya S, Sun X, Hu SY, Chen LQ. Philos Mag Lett 2011;91:110.
[28] Anand L, Gurtin ME. J Mech Phys Solids 2003;51:1015.
[29] Balluffi RW, Allen SM, Carter WC. Kinetics of materials. Hoboken, NJ: John Wiley; 2005.